SCIENCE CHINA
Earth Sciences

•ARTICLE•

September 2023 Vol.66 No.9: 1979–1993
https://doi.org/10.1007/s11430-022-1100-3

Long-term seismic network in South China Sea by floating MERMAIDs

Yong YU[1,2], Yongshun John CHEN[1,2*], Zhen GUO[1] & Zengxi GE[3]

[1] *Department of Ocean Science and Engineering, Southern University of Science and Technology, Shenzhen 518055, China;*
[2] *Southern Marine Science and Engineering Guangdong Laboratory (Guangzhou), Guangzhou 511458, China;*
[3] *School of Earth and Space Science, Peking University, Beijing 100871, China*

Received November 4, 2022; revised February 25, 2023; accepted April 3, 2023; published online July 25, 2023

Abstract Seismic data coverage in ocean regions is sparse, and it is highly challenging to build long-term continuous seismic networks in the oceans due to the restrictions related to the shortage of instruments and great costs. The lack of data coverage limits effective seismic imaging of deep mantle structures beneath the oceans, which cover 70% of the Earth's surface. The newly developed Mobile Earthquake Recorder in Marine Areas by Independent Drivers (MERMAID) can drift with ocean currents at a specified depth while recording seismic signals. The Southern University of Science and Technology (SUSTech) launched 10 MERMAIDs in the South China Sea (SCS) in May 2021 that formed the South China Sea Floating Seismic Network (SCS-FSN). We analyzed the one-year-long records of the SCS-FSN, identifying 372 cataloged earthquakes and acquiring 1,015 high-quality travel time data. By analyzing the records of earthquakes with magnitudes above 7.0 and conducting synthetic waveform calculation, we found that, in addition to the epicentral distance and earthquake magnitude, the earthquake identification ability of the network is also affected by the focal mechanism, sea condition, seafloor relief, and MERMAID working state. Although the recognition rate of the SCS-FSN is only 16% for earthquakes with magnitudes above 5.5 and epicentral distances less than 90°, this network is expected to collect more than 5,000 high-quality travel time data during its five-year battery life. These new data will significantly improve the seismic data coverage, compensating for the lack of long-term continuous seismic network observations in the SCS. Most importantly, with this experiment, we are confident that setting up well-designed floating seismic networks in the world's three oceans could solve the world-class problem of the lack of effective seismic data coverage beneath ocean regions.

Keywords South China Sea, MERMAID, Floating seismic network, Earthquake identification, Seismic data coverage

Citation: Yu Y, Chen Y J, Guo Z, Ge Z. 2023. Long-term seismic network in South China Sea by floating MERMAIDs. Science China Earth Sciences, 66(9): 1979–1993, https://doi.org/10.1007/s11430-022-1100-3

1. Introduction

The World-Wide Standardized Seismograph Network (WWSSN), the Global Digital Seismic Network (GDSN), the Global Seismographic Network (GSN), and other global seismic observation networks have been utilized to monitor nuclear explosion tests since the 1960s. Moreover, these networks have provided direct observations for geophysicists to research the global seismicity and focal mechanisms (Dziewonski et al., 1981; Ekström et al., 2012) and three-dimensional structures of the Earth's interior. These studies have provided substantial evidence for exploring the mechanism of plate tectonics, such as mantle plumes and plate subduction, promoting knowledge of the tectonic evolutionary history and internal state of the earth (e.g., Dziewonski et al., 1977; van der Hilst et al., 1997; Grand, 2002; Romanowicz, 2003; Montelli et al., 2004). Dense regional seismic networks (e.g., China National Seismic Network,

* Corresponding author (email: johnyc@sustech.edu.cn)

http://www.seisdmc.ac.cn) and temporary seismic arrays are sensitive for local earthquake detection, supplementing the local earthquake catalog and improving the accuracy of hypocenter locations (e.g., Xu and Gao, 2014). More importantly, dense seismic observations can improve the tomographic resolution of deep structures (e.g., Huang and Zhao, 2006; Shen et al., 2016; Han et al., 2021). In recent years, the deployment of large-scale and dense temporary seismic arrays on the continent, such as the China Seismic Science Array (ChinArray; China Array, 2006) and USArray (http://www.usarray.org), has provided abundant and reliable observations for imaging high-resolution seismic velocity structures deep beneath the Chinese continent and North America continent (e.g., Schmandt and Lin, 2014; Zhang et al., 2018; Huang et al., 2019). Meanwhile, ocean bottom seismometer (OBS) arrays have significantly promoted research on deep structures beneath ocean regions, such as the Hawaiian Plume-Lithosphere Undersea Melt Experience (PLUME; Wolfe et al., 2009) and Réunion Hotspot and Upper Mantle-Réunions Unter Mantle Experience (RHUM-RUM; Tsekhmistrenko et al., 2021), which unveil the structural characteristics of mantle plumes, and the Pacific OBS Research into Convecting Asthenosphere Experience (ORCA; Eilon et al., 2021), which reveals small-scale convection beneath the oceanic lithosphere. Moreover, the OBS observation array plays a crucial role in exploring subducting slab structures (e.g., Southern Mariana OBS Experience; Le et al., 2017; Zhu et al., 2019, 2020, 2021) and ocean basin evolution (Ruan et al., 2012; Liu et al., 2014; Wei et al., 2015; Xiao et al., 2017). However, the ocean area is much larger than that of the continent. Compared with continental seismic observations, it is challenging and costly to carry out analogously dense and long-term seismic networks due to the high manufacturing cost, high launch and recovery costs of OBSs, and unstable recovery rate of instruments and data. Restricted by sparse seismic observations, the imaging resolution of deep structures under ocean regions in global tomography is low (Zhao, 2004; Li et al., 2008; Simmons et al., 2012), hindering the understanding of key interior tectonic activities. For the SALSA3D global P-wave velocity model, the length of cells in the lower mantle beneath ocean regions (~8°) is more than four times that beneath the continent (<2°) to ensure the reliability and stability of the inversion (Ballard et al., 2016). In the checkerboard test of the LLNL-G3Dv3 model, the resolution under ocean regions is also very low (Simmons et al., 2012). Therefore, the construction of a long-term and stable seismic network to collect data in ocean regions can effectively advance the understanding of deep structures underneath.

The Mobile Earthquake Recorder in Marine Areas by Independent Drivers (MERMAID) is a newly developed seismometer that floats at a certain depth underwater, moves with ocean currents, and transmits data via satellite in near real-time (Simons et al., 2009). One MERMAID can identify and record seismic signals at different locations, effectively improving the data coverage in ocean regions. Referring to the trajectories of the ARGO (Array for Real-time Geologic Oceanography) floats (Davis et al., 2001), the simulation shows that records from 300 MERMAIDs that are uniformly deployed in ocean regions for five years can cover the entire space at deep depths. The five-year-long data recorded by 1,000 MERMAIDs can improve the resolution of body-wave tomography in the deep mantle under ocean regions to ~200 km (Sukhovich et al., 2015). Nolet et al. (2019) use only two-year-long data from 9 MERMAIDs to image the structures of the Galapagos mantle plume, significantly improving the tomographic resolution beneath the ocean side.

EarthScope-Oceans (www.earthscopeoceans.org) is an international cooperative research organization (Chen and Nolet, 2016) established in 2016. Its primary members are from Princeton University, the Southern University of Science and Technology (SUSTech), the University of Nice, and the Japan Institute for Marine Research and Development (JAMSTEC). EarthScope-Oceans aims to collect long-term and stable seismic observations, realizing intensive seismic observations in ocean areas using MERMAIDs. The SPPIM (South Pacific Plume Imaging with MERMAID) project is the first cooperative project of the EarthScope-Oceans. Fifty MERMAIDs (23 units from SUSTech, 16 from Princeton University, 9 from JAMSTEC/Kobe University, and 2 from the University of Nice) were launched in 2018 and 2019, establishing the South Pacific floating seismic network to image the mantle structure under the South Pacific. Pipatprathanporn and Simons (2021) identify 213 earthquakes (>M4.5) in one-year-long continuous data recorded by a salvaged MERMAID, and only 10 with magnitudes above 6.0 are transmitted via satellite. Simon et al. (2021b) find that the average earthquake recognition rates of MERMAID for earthquakes with magnitudes ranging from 5.0 to 5.9, 6.0 to 6.9, 7.0 to 7.9, and larger than 8.0 are ~0.5%, ~9.5%, ~44%, and ~81%, respectively. It is estimated that each MERMAID would identify 136 earthquake events with magnitudes above 5.0 on average in five years (Simon et al., 2021b). Since the statistical result does not consider other factors, such as the epicentral distance and focal mechanism, the above recognition rates may not reflect the actual value of MERMAID in seismic tomography.

In May 2021, SUSTech launched 10 MERMAIDs in the South China Sea (SCS), establishing the South China Sea Floating Seismic Network (SCS-FSN). We calculated statistics for one-year-long data of the network and analyzed signals of earthquakes with magnitudes above 7.0 to determine the possible influencing factors for earthquake detection via MERMAID. Our results further clarify the application value of the floating seismic network (FSN) in seismic tomography and earthquake monitoring. Establish-

ing the SCS-FSN can provide abundant seismic observations for imaging deep structures, compensating for the lack of long-term continuous seismic network observations in the SCS.

2. Working principle of MERMAID

The work procedure of MERMAID is shown in Figure 1 (Bonnieux and Hello, 2019). (1) On the sea surface, MERMAID locates its position coordinates and calibrates the clock by GPS. It transmits the underwater status log and identified seismic signals back to the data center and receives new commands via satellite. (2) After completing satellite communication, the MERMAID descends to the specified working depth (~1500 m) according to the external pressure and begins to monitor and analyze signals. (3) After continuously working underwater for a period of time (~7 days) or identifying a distinct seismic signal, MERMAID ascends to the sea surface and repeats step (1). The lithium battery carried by MERMAID can maintain its continuous operation for approximately five years. Ding et al. (2019) introduced the technical features and module function design of floating submarine seismographs in detail.

MERMAID is equipped with a hydrophone with a frequency band of 0.1–10 Hz, and its sampling rate is 40 Hz. At the underwater working depth, MERMAID calculates the short-term-average to long-term-average ratio (STA/LTA; Allen, 1978) of the received signal in real time. When the STA/LTA reaches a set threshold, discrimination of the P wave (P-wave credibility; Sukhovich et al., 2011) is performed based on the relative distribution of the power in different wavelet domains (Sweldens, 1996), and the signal-to-noise ratio (SNR) of the signal is calculated. These two parameters are used to determine whether to raise MERMAID immediately (Bonnieux and Hello, 2019). These parameters also determine the length of the transmitted data. When the P-wave credibility and SNR are low, the end of the transmitted data is 4,000 sampling points after the point where the STA/LTA rises to the set value. If the P-wave credibility and SNR are high, its end is 4,000 sampling points after the point where the STA/LTA decreases to the set value. Since MERMAID moves with ocean currents and can work continuously for five years, an FSN consisting of MERMAIDs can provide abundant seismic observations for tomography of mantle structures beneath ocean regions.

3. Data from the South China Sea floating seismic network

Supported by the National Natural Science Foundation of China (NSFC) Open Research Cruise, SUSTech deployed 10 MERMAIDs in the SCS in May 2021 (Figure 2a), establishing the SCS-FSN to explore deep mantle structures beneath the SCS. The floating times and drifting distances of the 10 MERMAIDs through May 2022 are shown in Table 1. The average drifting speed was ~2.3 km/day. MERMAID-63 drifted the longest distance in 368 days, 1,219 km, while MERMAID-71 drifted the shortest distance, 563 km in 381 days. MERMAID-67 stopped working in February 2022 and is believed to have been captured by a fishing boat while surfacing, as inferred from the status file. A total of 1,394 signals were transmitted by the 10 MERMAIDs via satellite. Each transmitted signal was matched with all possible earthquakes from the IRIS earthquake catalog during that

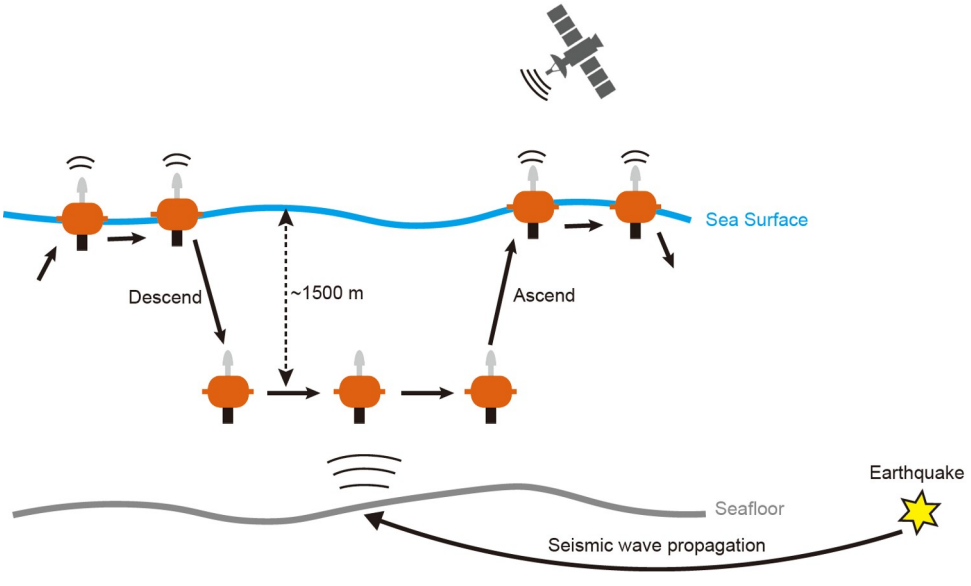

Figure 1 Schematic diagram of the working principle of MERMAID.

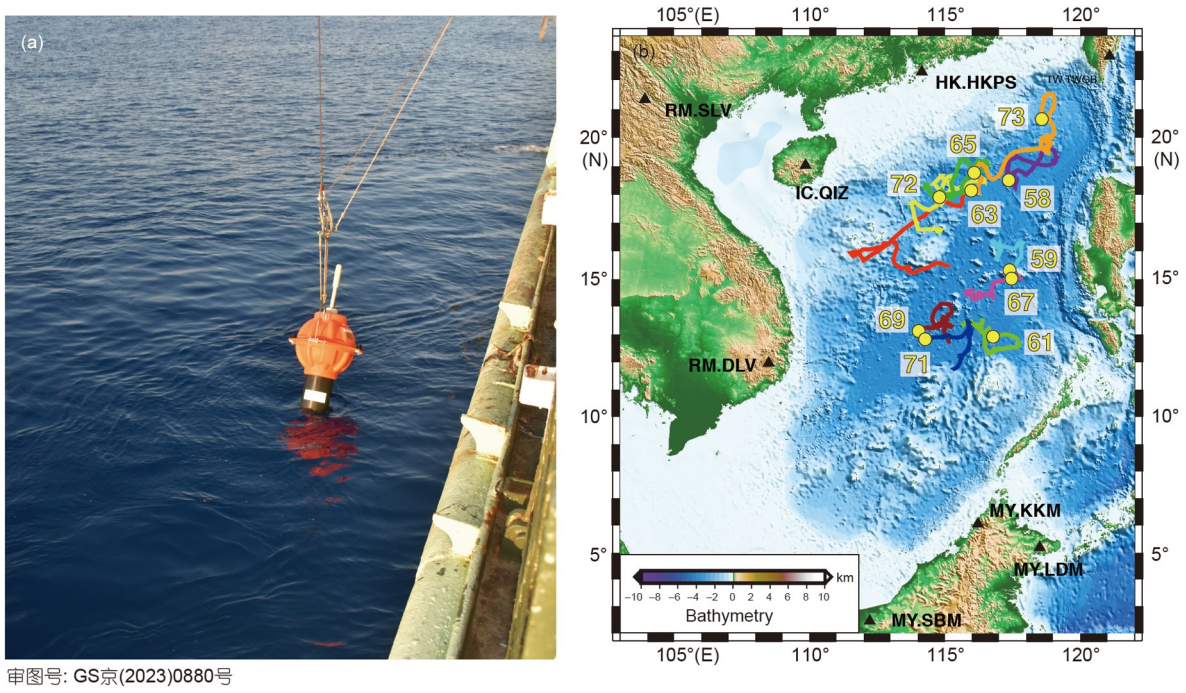

Figure 2 (a) Photograph of deploying MERMAID-65 on board R/V "SHIYAN 2"; (b) drifting tracks of MERMAIDs and locations of permanent stations onshore.

Table 1 Statistical table of the SCS-FSN recordings

ID	Launching date	Latest surfacing date	Drifting distance (km)	Received data	Cataloged signal	Uncatalogued signal
58	2021-05-20	2022-05-11	803.62	122	71	51
59	2021-05-12	2022-05-19	577.7	221	164	57
61	2021-05-11	2022-05-17	619.01	178	142	36
63	2021-05-02	2022-05-05	1,218.85	82	65	17
65	2021-05-01	2022-05-12	1,125.65	119	75	44
67	2021-05-11	2022-02-17	990.43	109	90	19
69	2021-05-03	2022-05-17	635.18	169	140	29
71	2021-05-03	2022-05-19	563.2	184	137	47
72	2021-04-30	2022-05-12	852.16	96	60	36
73	2021-05-12	2022-05-19	1,073.44	114	71	43
Total	–	–	–	1,394	1,015	379

period. The first arrival of a signal was determined in different wavelet domains based on the Akaike information criterion (AIC; Simon et al., 2020), which was then manually matched with the corresponding seismic phase (Appendix Figure S1, https://link.springer.com). Finally, 1,015 signals from 372 earthquakes were matched (Table 1, Figure 3a). The magnitudes of the matched earthquakes were mainly distributed between 5.5 and 7.5, and the epicentral distances were mainly distributed within 30°. The magnitudes of earthquakes with epicentral distances larger than 30° are generally above 5.0 (Figure 3b). In addition, 379 signals that could not be associated with cataloged earthquake events might come from regional earthquakes with epicentral distances less than 30° and magnitudes less than 4.5. The number of earthquakes identified by MERMAIDs in the southeastern SCS near the Philippine subduction zone is slightly greater than that in the northern SCS near the South China Block (Figure 3c). Since the data have been filtered strictly before being transmitted, the received MERMAID data have high SNRs and obvious onsets (p wave, P wave, and PKIKP wave; Figure 4), ensuring high-quality travel time measurement. The MERMAID records have SNRs similar to those of the velocity waveforms from continental permanent seismic stations. Since the record of the MERMAID hydrophone is water pressure, which is equivalent to an accelerometer at the frequency band of 0.1–10 Hz (Ian-

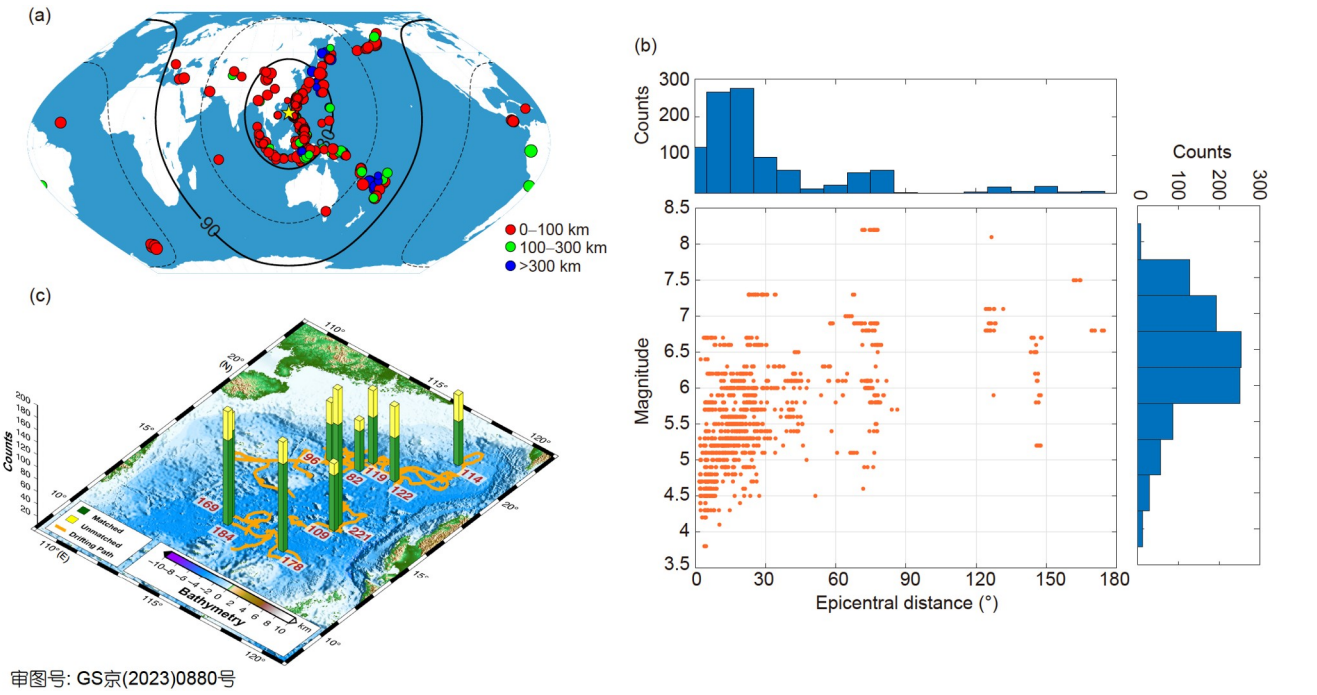

Figure 3 Statistical figures of earthquakes recorded by the SCS-FSN. (a) The yellow star represents the center of the network; the color-coded circles represent locations of earthquakes matched with the IRIS earthquake catalog. (b) The magnitude and epicentral distance distributions of matched earthquakes. The subplot on top is a histogram of epicentral distances, and the subplot on the right is a histogram of magnitudes. (c) Histogram of matched earthquakes of each MERMAID. The red numbers represent the quantities of matched MERMAID earthquakes, and the yellow numbers represent the quantities of unmatched signals.

naccone et al., 2020), the phase and amplitude of the waveform are different from those of the broadband seismograph onshore, which records the ground motion velocity (Figure 4). In addition to the first P-wave arrival, MERMAID can record the Sp converted at the seabed, T-wave, and Rayleigh surface wave (Figure 4b; Simon et al., 2021a). However, since the data transmitted by MERMAID are short, these seismic phases can only be observed when the epicentral distance is short.

Since the objective of the FSN is to image deep mantle structures inside the Earth, it is essential to evaluate the recognition rate of the network for earthquakes that are qualified for seismic tomography. Referring to the earthquake catalog of IRIS, we estimated the earthquake recognition rates of the 10 MERMAIDs in six epicentral distance intervals: <10°, <30°, <60°, <90°, 90°–120°, and >120° (Appendix Tables S1–S3, Figure 5a). The recognition rates of MERMAIDs for earthquakes with magnitudes in the ranges of 5.0–5.9, 6.0–6.9, and ≥7.0 are 2.6%, 23.6%, and 39.0%, respectively. The recognition rate in the same magnitude range decreases with increasing epicentral distance. For earthquakes with magnitudes between 5.0 and 5.9 and epicentral distances less than 10°, the recognition rate of MERMAIDs can reach 22.0%, while the recognition rate decreases to 4.0% for earthquakes with epicentral distances less than 90°. In the earthquake magnitude range of 6.0–6.9, the recognition rate is 48.1% for earthquakes with epicentral distances less than 10°, while that for earthquakes with epicentral distances less than 90° decreases to 29.9%, and the recognition rate decreases to 9.5% with epicentral distances larger than 120°. For earthquakes with magnitudes larger than 7.0, the MERMAIDs can identify 60.0% with epicentral distances less than 90° and 18.3% with epicentral distances larger than 120°. For earthquakes with epicentral distances between 90° and 120°, the recognition rate is 0% since the first arrival is the Pdiff wave, which grazes the core-mantle boundary (CMB; Figure 5b) and is generally picked up at low-frequency bands (~50 mHz; Kárason and van der Hilst, 2001). Therefore, the MERMAID hydrophone with a dominant frequency band of 0.1–10 Hz cannot identify the Pdiff wave well; thus, no data were identified within that epicentral distance range. Earthquakes with magnitudes larger than 5.5 and epicentral distances less than 90° are commonly measured in teleseismic body-wave tomography. The recognition rate of MERMAIDs is 16.0% for these earthquakes, and 9.5% with epicentral distances between 30° and 90° (Appendix Table S4, Figure 5a).

4. Discussion

The earthquake magnitude reflects the intensity of the released energy, and the epicentral distance determines the seismic ray path and geometric spreading coefficient of the

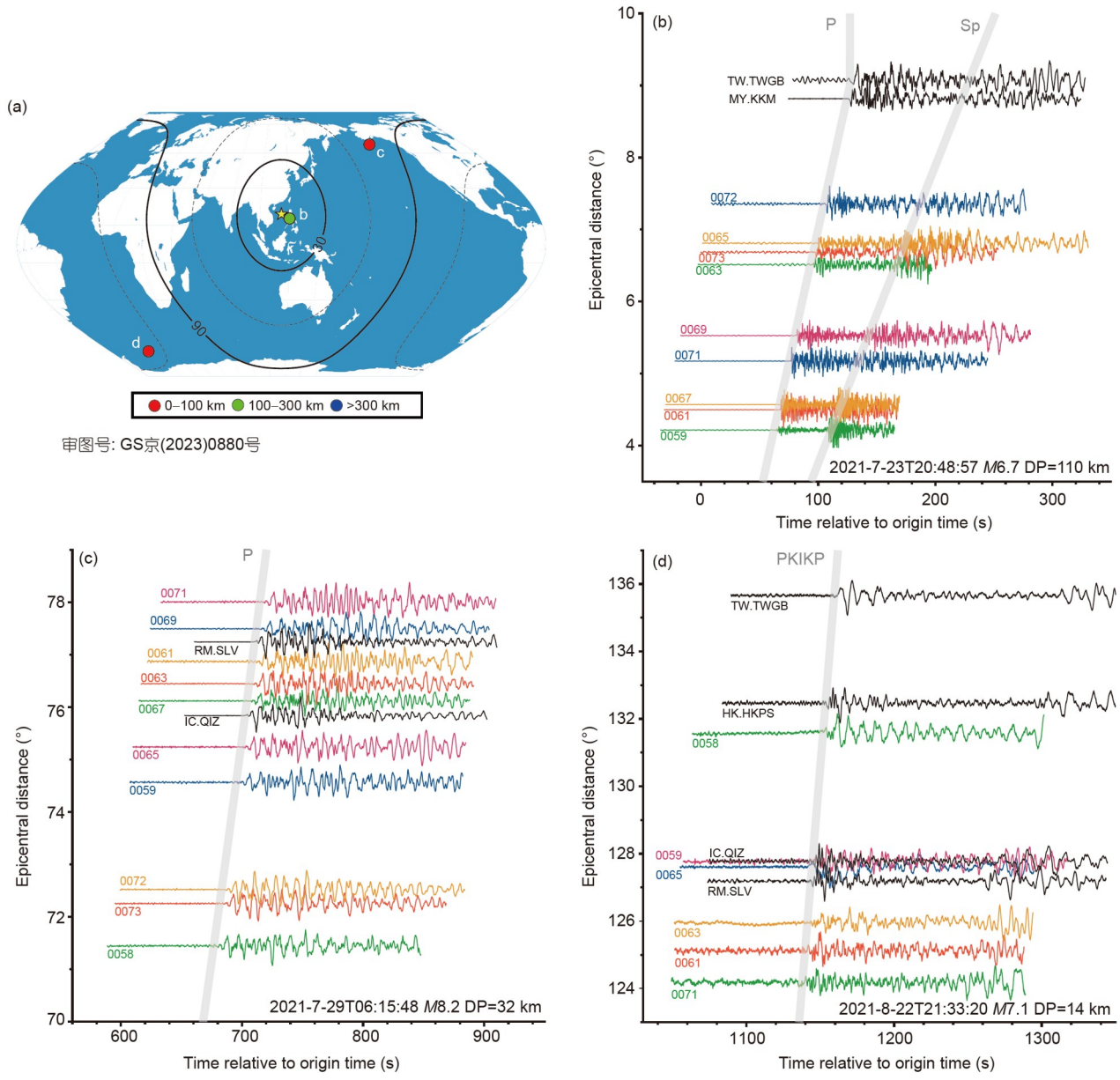

Figure 4 Earthquake waveforms with different epicentral distances recorded by the SCS-FSN. (a) shows the positions of earthquakes in (b)–(d). The solid gray lines represent the theoretical arrival times calculated based on the IASP91 velocity reference model (Kennett and Engdahl, 1991). The solid black lines represent the ground velocity waveforms of nearby onshore seismic stations after removing the instrument response via high-pass filtering at 0.1 Hz, and the colored lines represent the original waveforms of MERMAIDs.

first arrival. These two parameters affect the amplitude of the onset recorded by MERMAID, impacting the STA/LTA and SNR of the signal. However, even though the epicentral distance of the same teleseismic event for the network is similar, some MERMAIDs cannot identify the event while others can transmit clear signals. To determine what other factors affect the recognition of earthquakes, we analyzed the records of 12 earthquakes with magnitudes above 7.0 that occurred in one year (Appendix Figure S2) and discussed other possible factors that might affect the recognition of earthquakes. Finally, we demonstrated the application value and prospects of the FSN in seismic tomography and monitoring.

4.1 Influence factors of earthquake recognition

4.1.1 Focal mechanism and preorder signal

Referring to the double-couple earthquake focal mechanism, the amplitude and polarity of the onset vary with the back azimuth and epicentral distance. The M_w7.5 and M_w8.1 earthquakes occurring near the South Sandwich Islands on 2021-08-12T18:32 and 2021-08-12T18:35 were identified only by MERMAID-61. Since the origins of the two events are close, the PKIKP wave of the latter is submerged by the coda of the previous earthquake. The records of MERMAID-61 and continental seismic stations show that the PKIKP

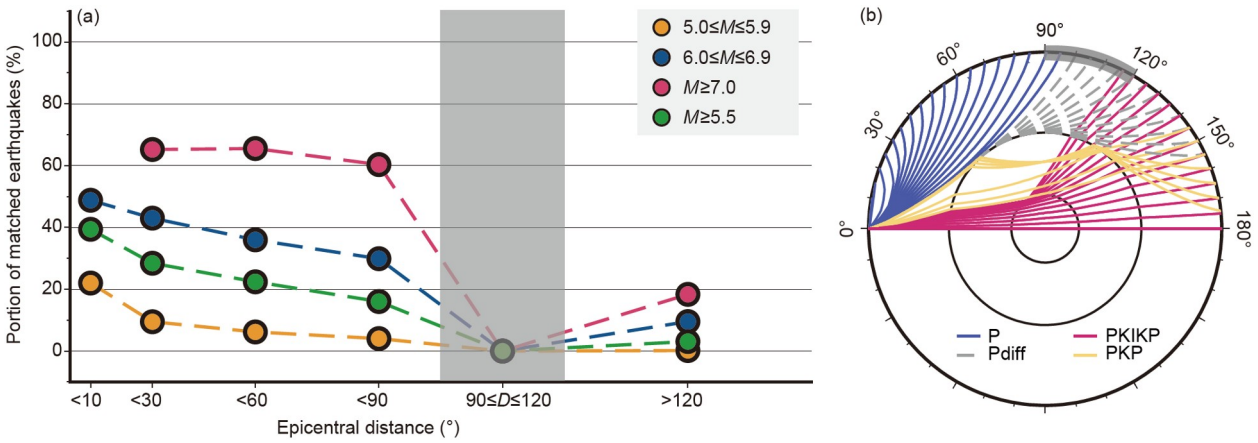

Figure 5 (a) The portions of earthquakes identified by the MERMAIDs and matched with the IRIS earthquake catalog in different magnitude and epicentral distance ranges. The gray area covers the epicentral distance range of 90°–120°. (b) Ray paths of the P, Pdiff, PKIKP, and PKP waves with different epicentral distances. The gray area indicates that the first arrival is unclear at high-frequency bands.

wave of the M_w7.5 earthquake is spindle-shaped (Figure 6). The projections of the PKIKP wave of the 10 MERMAIDs on the focal sphere are located near the fault or auxiliary plane, leading to weak P-wave amplitudes. In addition, the half duration (HD) of the source-time function (STF) of this earthquake is 150 s, which also results in a small amplitude at high-frequency bands at a long distance (Kanamori, 1974). Thus, the STA/LTA of the signal estimated by the MERMAIDs was suppressed, falling below the set threshold. Pipatprathanporn and Simons (2021) analyzed continuous one-year-long data of salvaged MERMAID records. They also found that MERMAID did not recognize some earthquakes with unambiguous onsets, despite the strong energies. Therefore, in addition to the magnitude and epicentral distance, the projection location of MERMAID on the focal sphere and the STF also affect its identification of earthquakes.

In addition to the M_w8.1 earthquake mentioned above, the PKIKP wave of the M_w7.2 earthquake occurring near Haiti on 2021-08-14T12:29 can be observed in the records of the seismic stations near the SCS when the epicentral distance is less than 143°. Beyond that distance, the PKIKP wave is submerged in the preorder signal (Figure 6), decreasing the STA/LTA and SNR below the threshold and impeding the earthquake identification of MERMAID-72 and MERMAID-73.

4.1.2 Ascent and descent of MERMAID

MERMAID does not record signals while surfacing or diving, losing signals arriving during the period, which is the main factor that obstructs the identification and transmission of earthquake signals with magnitudes above 7.0. The recognition rate of the SCS-FSN is 60.3% for earthquakes with epicentral distances less than 90° and 18.3% for epicentral distances larger than 120°. According to statistical results, 25 earthquake events are missed due to the ascent and descent of the 10 MERMAIDs. The epicentral distances of 17 events are less than 90°, accounting for ~74% of the total missing events within that epicentral distance range. Ignoring the missing events due to this factor, the recognition rate of the SCS-FSN can reach ~90% for earthquakes with magnitudes above 7.0 and epicentral distances less than 90°. The processes of ascent, descent, and communication with the satellite on the sea surface take ~17 h in total in one work cycle. The time duration of a work cycle must be considered in three cases. (1) MERMAID completes a work cycle of ~7 days. The nonrecorded time accounts for ~9.1% of the cycle, and five missing events occur in this case. (2) MERMAID floats up immediately when it records a signal with a high SNR and P-wave credibility, and the proportion of nonrecording time is higher than that of the former case. Seventeen missing events are due to this case. (3) MERMAID triggers emergency surfacing immediately when touching the seafloor if the water depth is shallower than the working depth and sends a warning of adjusting parameters to the data center. In this case, MERMAID does not record any data. Considering the shallow water depth, the working depth of MERMAID-63 was set to 750 m, but it still touched the seafloor near the Zhongsha Atoll and floated up frequently from December 2021 to March 2022, resulting in the omission of three earthquake signals with magnitudes above 7.0.

Although extending the time length of the MERMAID work cycle can effectively reduce the proportion of nonrecording time, it might also reduce the estimation accuracy of the position and clock, increasing the uncertainty of travel time measurements. The position of the MERMAID underwater is estimated via linear interpolation. The simulation results show that the travel time errors caused by the position interpolation are less than 0.3 s, and ~67% are less than 0.05 s, which is acceptable in travel time seismic tomography (Joubert et al., 2015). However, the error increases as the interpolation interval becomes longer. A short work cycle

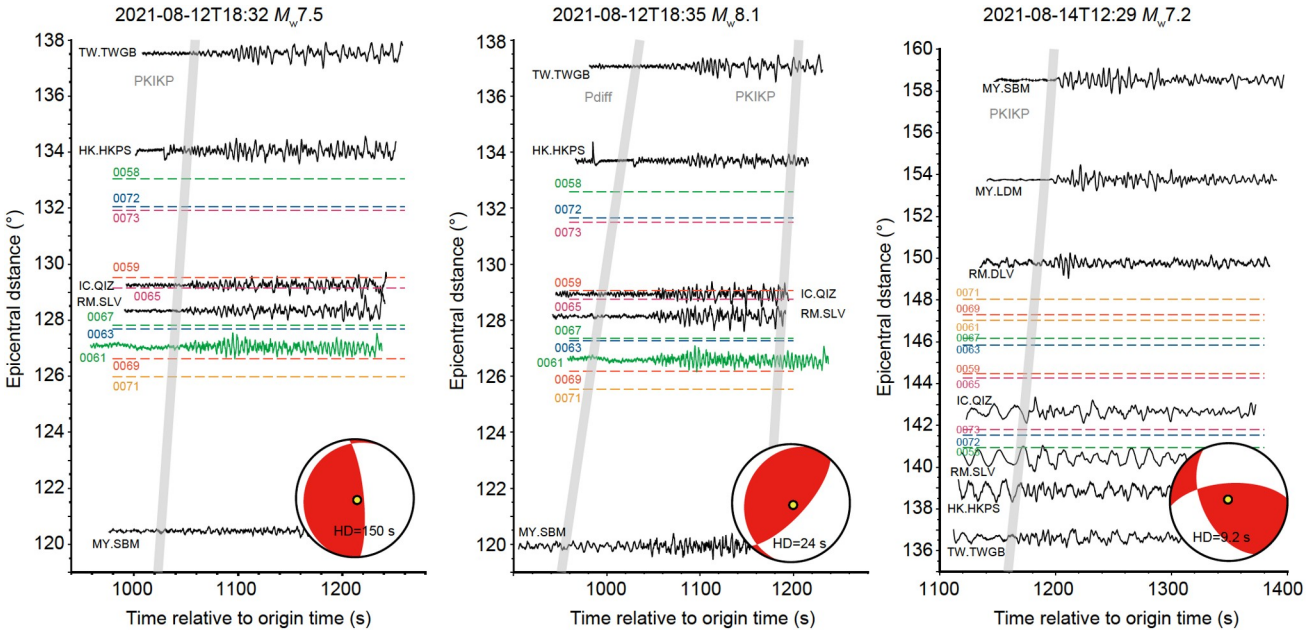

Figure 6 Influence of the focal mechanism and preorder signal on the waveform. The waveforms recorded by continental permanent seismic stations (solid black lines) are ground velocity after removing the instrument response and with a high-pass filter of 0.1 Hz. The locations of these stations are shown in Figure 2b. For comparison, the reference time in the middle subplot is the same as that in the right subplot. The colored dashed lines indicate that the MERMAID did not recognize the earthquake, and the location of the MERMAID at the origin time of the earthquake is estimated. The solid gray lines are the theoretical arrival times calculated based on the IASP91 reference model (Kennett and Engdahl, 1991). The focal mechanism solutions are from the GCMT catalog (Dziewonski et al., 1981; Ekström et al., 2012). The yellow dots are the projections of MERMAIDs on the focal sphere. HD is short for the half duration.

can reduce the error of the estimated position, but it could increase the proportion of nonrecording time and shorten the battery life of MERMAID due to the frequent operation of the oil pump. The work cycle of MERMAID in the SCS-FSN is seven days and can be maintained for five years while ensuring the quality and accuracy of travel time measurements.

4.1.3 Sea condition

The M_w7.5 earthquake occurring near Peru on 2021-11-28T10:52 was identified by only four MERMAIDs (59, 61, 67, and 71) located in the southeastern SCS, while the other MERMAIDs in the central and northern SCS failed to recognize it (Figure 7a). We requested the records of four of the unrecognized MERMAIDs (58, 69, 72, and 73) around the earthquake arrival time via satellite (Figure 7b). Regarding the time windows of 40 s before and after the PKIKP-wave theoretical arrival time as the noise and earthquake signal, respectively, we calculated their power spectra and SNRs. The SNRs of the four MERMAIDs that identified the earthquake were between 5.0 and 9.8, while the SNRs of the other four unidentified MERMAIDs were less than 3.0. Thus, the reduction in SNR is the main reason why the earthquake was not recognized. The spectrum intensities of the eight MERMAIDs are similar in the earthquake-signal time window (Figure 7c). However, the noise spectrum intensities of the four unidentified MERMAIDs are higher in the frequency band of 0.2–1.0 Hz (Figure 7c). Therefore, the reduction in SNR may be caused by the enhancement of ambient noise.

The main source of seismic ambient noise is sea waves. Noise below 0.1 Hz is generated mainly by the interaction of sea waves and seafloor; noise above 0.1 Hz is attributed mainly to the interaction of sea waves on the surface (Ardhuin et al., 2019). Pipatprathanporn and Simons (2021) confirm that the interaction between the atmosphere and water on the sea surface is the main source of infrasound waves at a depth of 1500 m by comparing the noise signals recorded by MERMAID with the simulation based on the WAVEWATCH III wave-height model. On November 28, 2021, the China Ocean Prediction Network (http://www.oceanguide.org.cn) posted a blue wave warning (level IV/general) that the northeast wind force was 6–7, and the wave height was up to 3.5–5.5 m in the central and northern SCS. The unidentified MERMAIDs were located in areas with strong winds and high waves (Appendix Figure S3). We speculate that the strong wind and high waves on the sea surface enhanced the noise level in the recording frequency band of MERMAID, reducing the SNR and hindering the recognition of the earthquake. In addition to wave height, the shaking of MERMAIDs caused by current disturbance and variations in water depth and seafloor relief may also affect the amplitude of the received signal.

4.1.4 Seafloor relief and other factors

Changes in the topography can cause focusing and defo-

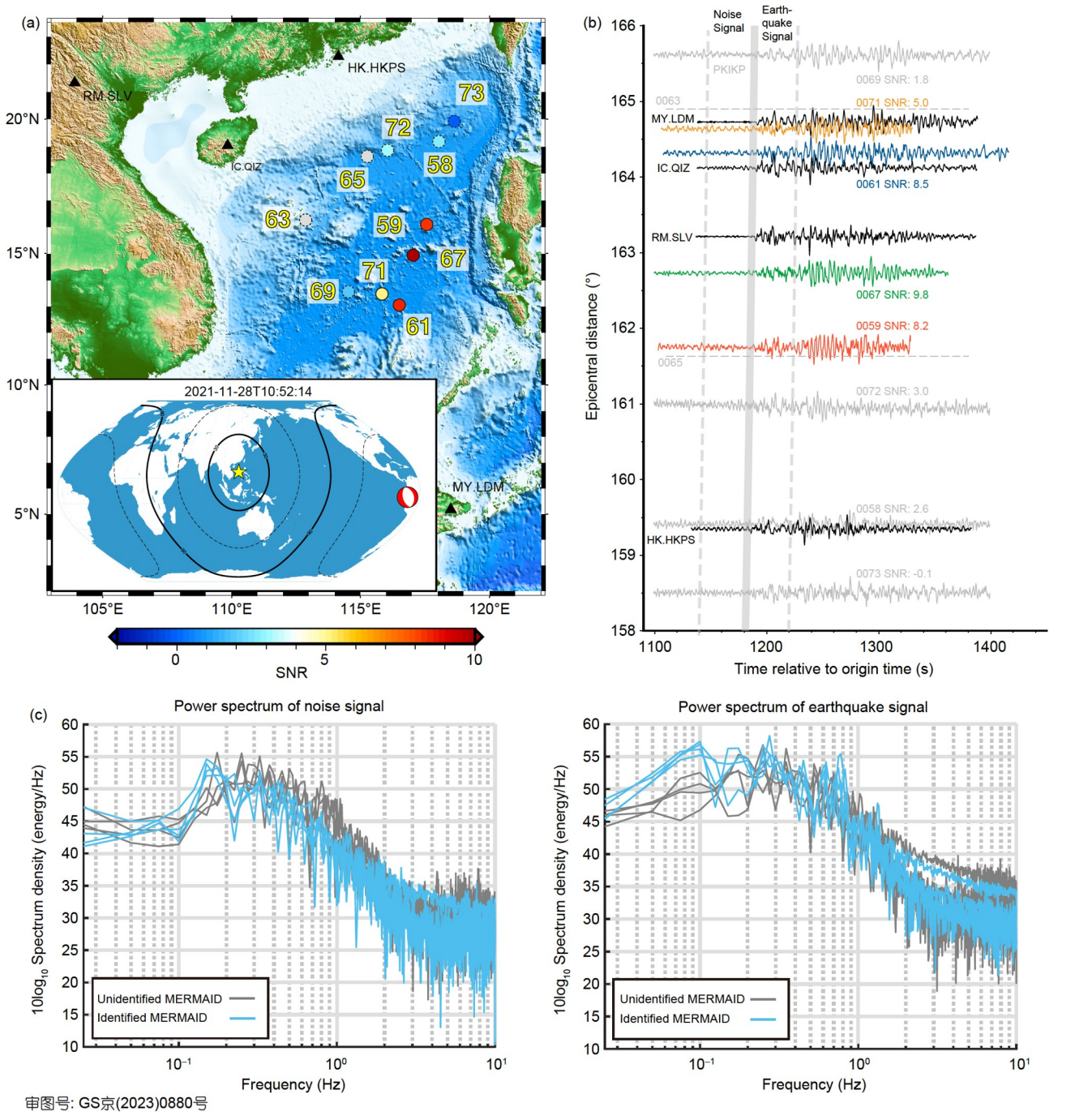

Figure 7 The SNR distribution, waveforms, and power spectra of the earthquake on 2021-11-28T10:52 recorded by the SCS-FSN. (a) The circles mark the estimated positions of MERMAIDs when the earthquake occurred. The color of the circles represents the SNR of the recorded signal, and MERMAIDs with no data are in gray. MERMAIDs plotted with solid edge lines identified the earthquake, while those with dashed edge lines failed. The lower-left corner subplot shows the location and focal mechanism of the earthquake. (b) The same as Figure 6. The waveforms of identified MERMAIDs are drawn with solid colored lines, and those of unidentified MERMAIDs are drawn with solid gray lines. The time windows of the noise and earthquake signal used for estimating the SNR are marked with gray dashed lines. (c) The power spectral density of the unfiltered signals in the noise and earthquake signal window of each MERMAID.

cusing of the seismic wavefield, affecting the spatial distribution of the wavefield energy, such as uplift, concavity (Boore, 1973; Bouchon, 1973), and step (Bouckovalas and Papadimitriou, 2005). Similarly, changes in the seafloor relief can affect the amplitude of signals recorded by a MERMAID drifting at a certain depth underwater. We used the boundary element method (BEM; Ge and Chen, 2008) to simulate 2-D wavefields with different types of seafloor relief (Appendix Figure S4) and evaluated the impact of seafloor relief on the signal received by MERMAID. The simulation results (Figure 8) show that the amplitudes of signals from MERMAIDs above the edges of the uplift,

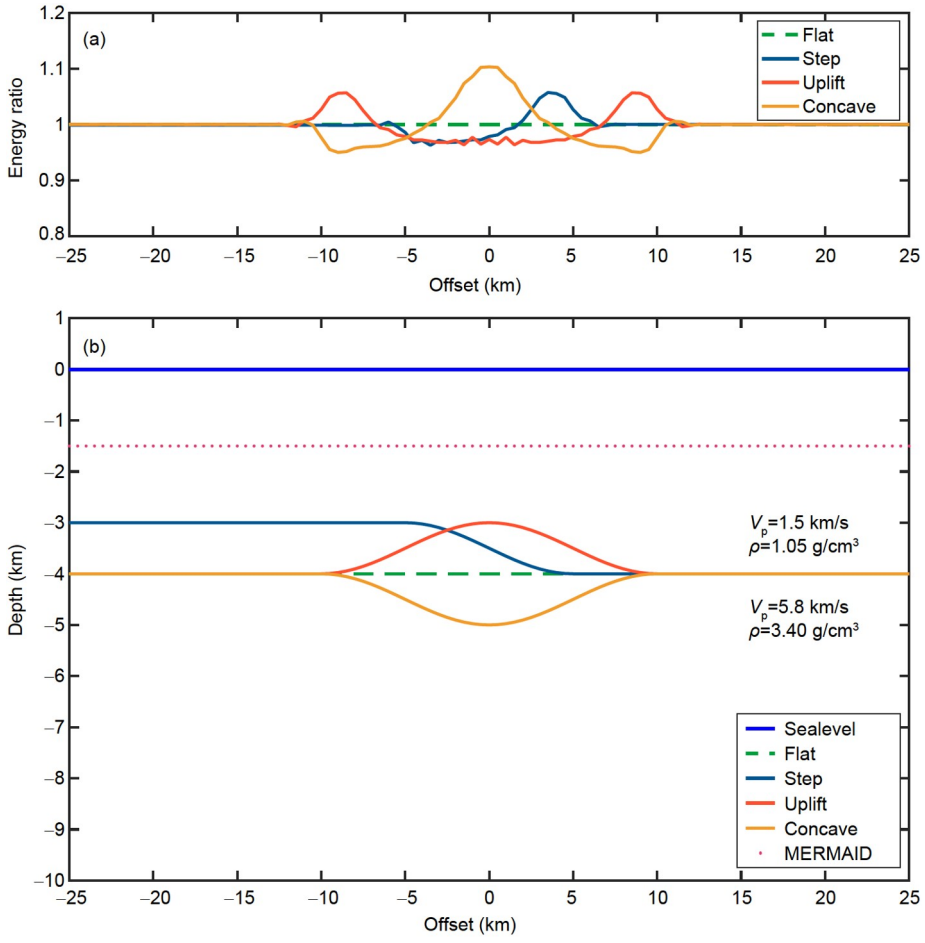

Figure 8 Relative amplitudes of simulated signals recorded by MERMAIDs above different types of seafloor relief. (a) The ratios of the maximum energies of the 5 s teleseismic waveforms recorded by MERMAIDs at 1.5 km depth in different horizontal positions (Appendix Figure S4) with different types of seafloor relief to those with flat seafloor relief, which were simulated by the BEM. (b) The parameter settings of the seafloor relief (flat, uplift, concave, and step).

bottom of the step, and middle of the concavity are significantly enhanced; those from MERMAIDs above the uplift, upper part of the step, and edges of the concavity are significantly weakened. Moreover, the gain effect could be strengthened after multiple reflections of sound waves in the water (Appendix Figure S5). Therefore, the amplitude of signals received by MERMAID could be impacted by the seafloor relief below, affecting the estimated SNR and earthquake identification.

The omission of some earthquake events by MERMAIDs cannot be explained by the above factors. Such as the failed identification of the M_w7.0 earthquake occurring in the southeast of the Loyalty Islands on 2022-03-31T05:44 by MERMAID-69, 72, and 73 and the failed identification of the M_w7.0 earthquake occurring near Mexico on 2021-09-08T01:47 by MERMAID-61, 63, 71, and 72. We manually requested and analyzed the records during the occurrence of these two earthquakes. The unidentified signals have high SNRs (>7), and some are even larger than 13 (Figure 9). We speculate that the omission of these signals is due to the low P-wave credibility. MERMAID uses the energy distribution of a signal in different wavelet domains to judge the P wave, but the judgment of this method is not completely correct. Reducing the rate of false negative recognition of the P wave could also lead to a decrease in the rate of true positive recognition (Sukhovich et al., 2011).

Lowering the thresholds of the STA/LTA, SNR, and P-wave credibility can improve the earthquake recognition rate of MERMAID, but it also increases the transmission of low SNR and nonseismic signals. The uncertainties of the travel time measurements on low-SNR signals are large, which are removed or only with small weights in tomographic inversion. Meanwhile, as the data transmission increases, the cost of satellite communication and power consumption increase, shortening the working life of a MERMAID. Therefore, lowering the identification thresholds might not increase the qualified measurements for tomography research, but on the contrary, the working life of MERMAID could be shortened, reducing the total quantity of high-quality transmitted data.

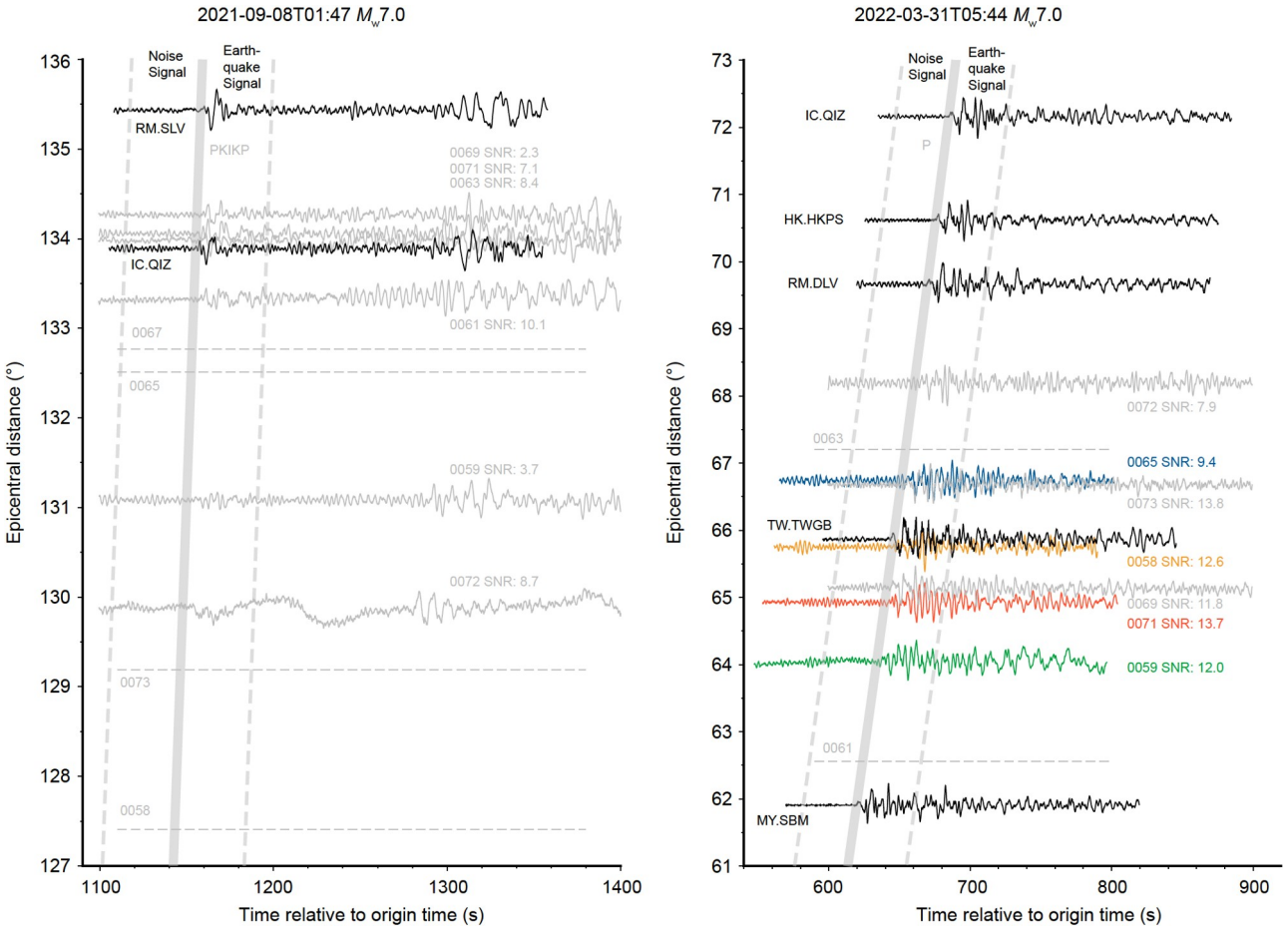

Figure 9 Waveforms of earthquakes that occurred on 2021-09-08T01:47 and 2022-03-31T05:44. The same as Figure 7b. The power spectra are shown in Appendix Figure S6.

4.2 Application of the SCS-FSN

The tomographic resolution below 500 km depth under the SCS is significantly lower than that of the surrounding area when only onshore seismic stations are adopted (Huang et al., 2015). We selected 11 permanent stations around the SCS available from the IRIS and calculated the P-phase ray paths of earthquakes with magnitudes above 5.5 and epicentral distances less than 90° and PKIKP-phase ray paths of earthquakes with magnitudes above 6.0 and epicentral distances larger than 120° between June 2021 and May 2022. The total number of ray paths is 3,758, and the ray coverage is sparse under the SCS (Figure 10a). Moreover, only high-quality travel time measurements with small uncertainties can be used in the inversion to ensure the reliability of the tomographic result. For example, in the measurement of P-wave travel time residuals recorded by national permanent seismic stations between January 2012 and January 2014 by Yu et al. (2021), only 133 earthquakes in the frequency band of 0.5–2.0 Hz were utilized in the inversion, while 365 earthquakes with magnitudes above 5.5 and epicentral distances between 30° and 90° occurred during that period. The utilization rate was 36.4%. Referring to the above result, the acceptable ray paths in the SCS might be less than 1,400, resulting in poor constraints on structures beneath the SCS if only permanent stations are used. The 1,015 seismic ray paths recorded by the SCS-FSN in one year could fill the gap in ray coverage (Figure 10b). Considering that the signals transmitted by MERMAID have high STA/LTA and SNR, most can satisfy the requirements of seismic tomography. It is estimated that during the five-year-long battery life, the SCS-FSN could collect ~5,000 high-quality travel time data, compensating for the lack of long-term continuous seismic networks in the SCS. It could provide valuable seismic observations for detecting deep mantle structures underneath.

In addition, the SCS-FSN identified a number of seismic signals occurring around the SCS which were not cataloged by the IRIS. For example, by searching the earthquake catalog of the European-Mediterranean Seismological Centre (EMSC), the *M*3.4 earthquake that occurred on 2021-08-20T12:44:53 near Mindoro Island and the *M*4.1 earthquake that occurred on 2021-08-22T09:13:50 near Luzon Island were matched. The signals were identified and transmitted by MERMAID-61 and MERMAID-63 and 69, respectively

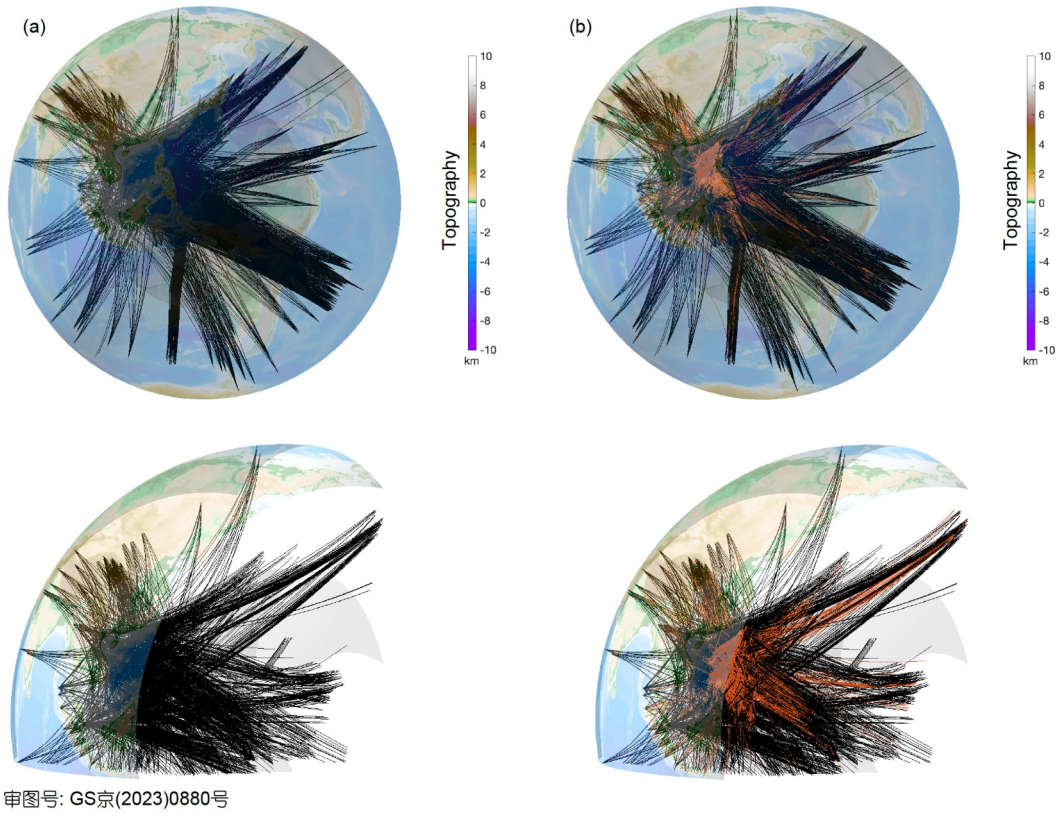

Figure 10 Ray path distribution of permanent stations and the SCS-FSN. The figures show the P-phase and PKIKP-phase ray paths of permanent stations from the IRIS around the SCS (a) and SCS-FSN (b) for one year (assuming all earthquakes are recorded). The bottom subplots are zoomed-in views of the SCS. The rays recorded by permanent stations (black) are drawn over those of the SCS-FSN.

(Figure 11). In addition to the direct P wave, the two MERMAIDs recorded the Sp wave of the latter earthquake, which was converted from an S to a P wave at the seafloor. Thus, the FSN can also provide an important supplement for the continental seismic network, complementing the azimuth coverage for monitoring and analyzing local earthquakes. Moreover, the SCS-FSN also identified some signals that have not been cataloged by the regional network and are difficult to locate since only a few MERMAIDs identified them (Figure 11). The distribution of seismicity is helpful in studying the deep structures of a subducting slab (e.g., Zhu et al., 2023). By increasing the number of MERMAIDs and reducing the identification thresholds, the earthquake detection ability of the FSN can be promoted. In addition, by combining with the traditional OBS array, the FSN can provide more observations for locating and monitoring small earthquakes. However, differences exist between the settings of MERMAID used for earthquake monitoring and seismic tomography, and the MERMAID parameters need to be adjusted according to the purpose.

5. Conclusion

We analyzed one-year-long data collected by the SCS-FSN, which consists of 10 MERMAIDs deployed by SUSTech. The analysis shows that the recognition rate of the SCS-FSN is ~11.2% for global earthquakes with magnitudes above 5.5 and increases to ~16.0% when the epicentral distance is less than 90°. The earthquake recognition of the network is affected by earthquake characteristics, such as the earthquake magnitude, epicentral distance, focal mechanism, rupture process, and other natural factors, such as the seafloor relief and sea condition. In addition, it is influenced by the ascent and descent process of MERMAIDs. However, even though the earthquake recognition rate of MERMAID is lower than the earthquake utilization rate of continental seismic networks for seismic tomography, the signals transmitted by MERMAID are high quality and have high SNRs, making up for the poor seismic data coverage of continental networks beneath ocean regions. Therefore, the FSN equipped with MERMAIDs can provide reliable and abundant seismic observations for imaging deep mantle structures beneath ocean regions. It can be inferred that the well-designed establishment of FSNs in the three oceans could solve the world-class challenge that ocean regions, which cover 70% of the Earth's surface, lack effective seismic data coverage. In addition, the FSN with appropriate settings can be used for long-term monitoring of small earthquakes in ocean regions.

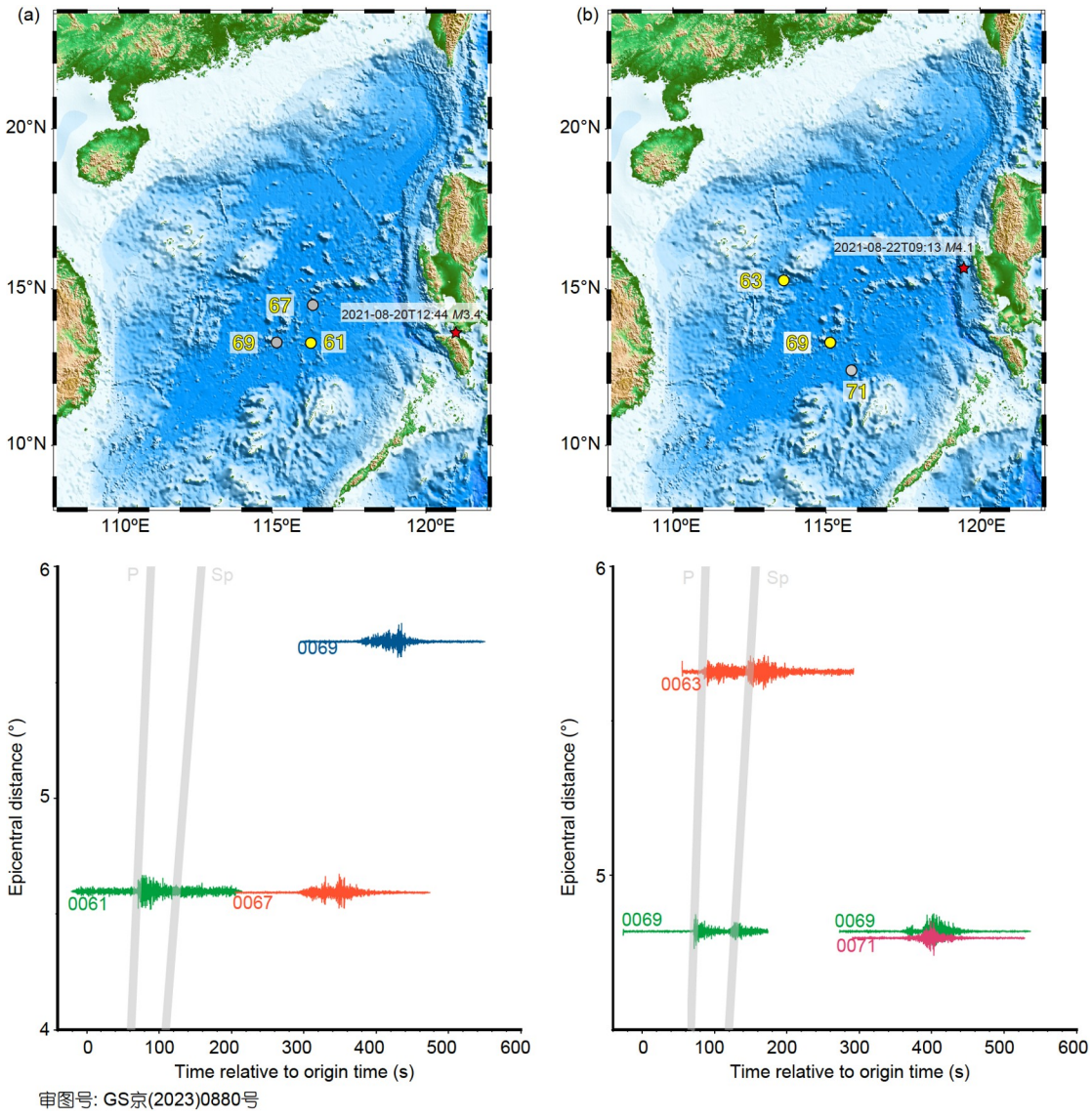

Figure 11 Waveforms recorded by MERMAIDs that are uncatalogued by the IRIS. The top subplots show the epicenters of small earthquakes from the earthquake catalog by EMSC and estimated locations of MERMAIDs, which transmitted data recorded near the origin time of earthquakes. The transmitted signals represented by gray circles cannot match the arrival times of the cataloged earthquakes. The bottom subplots show the theoretical arrival times of the cataloged earthquakes and waveforms transmitted by MERMAIDs.

Acknowledgements *The deployment of the 10 MERMAIDs was supported by the NSFC Open Research Cruise (Cruise No. NORC2021-08), funded by Shiptime Sharing Project of the NSFC. This cruise was conducted onboard R/V "SHIYAN 2" by the South China Sea Institute of Oceanology, Chinese Academy of Sciences. We thank the chief scientist Dr. Xuelin QIU, the captain Dr. Jiazheng ZHANG and all the staff onboard for their support and help. We appreciate the responsible editor and three reviewers for their valuable comments and suggestions. We thank Dr. Zhiqiang LIU from SUSTech for providing the wave height information of the South China Sea and Yizhi WANG for helping with the discussion of the working principle of the hydrophone. The software processing the MERMAID data can be downloaded at https://github.com/joelsimon/omnia/. The figures in this paper were plotted by Generic Mapping Tools (GMT) 6. The work was supported by the National Natural Science Foundation of China (Grant No. 41890814) and the Southern Marine Science and Engineering Guangdong Laboratory (Guangzhou).*

References

Allen R V. 1978. Automatic earthquake recognition and timing from single traces. Bull Seismol Soc Am, 68: 1521–1532

Ardhuin F, Gualtieri L, Stutzmann E, Nakata N, Fichtner A. 2019. Physics of ambient noise generation by ocean waves. In: Nakata N, Gualtieri L, Fichtner A, eds. Seismic Ambient Noise. Cambridge: Cambridge University Press. 69–108

Ballard S, Hipp J R, Begnaud M L, Young C J, Encarnacao A V, Chael E P, Phillips W S. 2016. SALSA3D: A tomographic model of compressional wave slowness in the Earth's mantle for improved travel-time prediction and travel-time prediction uncertainty. Bull Seismol Soc Amer, 106: 2900–2916

Bonnieux S, Hello Y. 2019. MERMAID Profiler: User Manual. Osean Technology Co., Ref: 452.010.852

Boore D M. 1973. The effect of simple topography on seismic waves: Implications for the accelerations recorded at Pacoima Dam, San Fer-

nando Valley, California. Bull Seismol Soc Amer, 63: 1603–1609
Bouchon M. 1973. Effect of topography on surface motion. Bull Seismol Soc Amer, 63: 615–632
Bouckovalas G D, Papadimitriou A G. 2005. Numerical evaluation of slope topography effects on seismic ground motion. Soil Dyn Earthq Eng, 25: 547–558
Chen Y J, Nolet G. 2016. A complete tomography of the Earth's interior with floating seismometers in the oceans: The EarthScope-Oceans. American Geophysical Union Fall Meeting, Abstract S31D-07
China Array. 2006. China Seismic Array Waveform Data. China Earthquake Administration, http://doi.org/10.12001/ChinArray.Data
Davis R E, Sherman J T, Dufour J. 2001. Profiling ALACEs and other advances in autonomous subsurface floats. J Atmos Ocean Technol, 18: 982–993
Ding W W, Huang H C, Zhu X K, Sun G Q, Niu X W. 2019. New mobile oceanic seismic recording system and its application in marine seismic exploration (in Chinese). Prog Geophys, 34: 292–296
Dziewonski A M, Chou T A, Woodhouse J H. 1981. Determination of earthquake source parameters from waveform data for studies of global and regional seismicity. J Geophys Res-Solid Earth, 86: 2825–2852
Dziewonski A M, Hager B H, O'Connell R J. 1977. Large-scale heterogeneities in the lower mantle. J Geophys Res-Solid Earth, 82: 239–255
Eilon Z C, Gaherty J B, Zhang L, Russell J, McPeak S, Phillips J, Forsyth D W, Ekström G. 2021. The Pacific OBS Research into Convecting Asthenosphere (ORCA) experiment. Seismol Res Lett, 93: 477–493
Ekström G, Nettles M, Dziewoński A M. 2012. The global CMT project 2004–2010: Centroid-moment tensors for 13,017 earthquakes. Phys Earth Planet Inter, 200-201: 1–9
Ge Z, Chen X. 2008. An efficient approach for simulating wave propagation with the boundary element method in multilayered media with irregular interfaces. Bull Seismol Soc Amer, 98: 3007–3016
Grand S P. 2002. Mantle shear-wave tomography and the fate of subducted slabs. Philos Trans R Soc Ser A, 360: 2475–2491
Han S, Zhang H, Xin H, Shen W, Yao H. 2021. USTClitho2.0: Updated unified seismic tomography models for continental china lithosphere from joint inversion of body-wave arrival times and surface-wave dispersion data. Seismol Res Lett, 93: 201–215
Huang J, Zhao D. 2006. High-resolution mantle tomography of China and surrounding regions. J Geophys Res-Solid Earth, 111: B09305
Huang Z, Wang L, Xu M, Zhao D, Mi N, Yu D. 2019. P and S wave tomography beneath the SE Tibetan Plateau: Evidence for lithospheric delamination. J Geophys Res-Solid Earth, 124: 10292–10308
Huang Z, Zhao D, Wang L. 2015. P wave tomography and anisotropy beneath Southeast Asia: Insight into mantle dynamics. J Geophys Res-Solid Earth, 120: 5154–5174
Iannaccone G, Pucciarelli G, Guardato S, Donnarumma G P, Macedonio G, Beranzoli L. 2020. When the hydrophone works as an accelerometer. Seismol Res Lett, 92: 365–377
Joubert C, Nolet G, Bonnieux S, Deschamps A, Dessa J, Hello Y. 2015. P-delays from floating seismometers (MERMAID), Part I: Data processing. Seismol Res Lett, 87: 73–80
Kanamori H. 1974. A new view of earthquakes. In: Kanamori H, Boschi E, eds. Physics of the Earth (A Modern View of the Earth) (in Japanese). Tokyo: Physical Society of Japan, Maruzen. 261–282
Kárason H, van der Hilst R D. 2001. Tomographic imaging of the lowermost mantle with differential times of refracted and diffracted core phases (PKP, P diff). J Geophys Res-Solid Earth, 106: 6569–6587
Kennett B L N, Engdahl E R. 1991. Traveltimes for global earthquake location and phase identification. Geophys J Int, 105: 429–465
Le B M, Lin J, Yang T, Shiyan3 S P O R. 2017. Southern mariana OBS experiment and preliminary results of passive-source investigations. American Geophysical Union Fall Meeting, Abstract OS53A-1159
Li C, van der Hilst R D, Engdahl E R, Burdick S. 2008. A new global model for P wave speed variations in Earth's mantle. Geochem Geophys Geosyst, 9: Q05018
Liu C, Hua Q, Pei Y, Yang T, Xia S, Xue M, Le B M, Huo D, Liu F, Huang H. 2014. Passive-source ocean bottom seismograph (OBS) array experiment in South China Sea and data quality analyses. Chin Sci Bull, 59: 4524–4535
Montelli R, Nolet G, Dahlen F A, Masters G, Engdahl E R, Hung S H. 2004. Finite-frequency tomography reveals a variety of plumes in the mantle. Science, 303: 338–343
Nolet G, Hello Y, Lee S, Bonnieux S, Ruiz M C, Pazmino N A, Deschamps A, Regnier M M, Font Y, Chen Y J, Simons F J. 2019. Imaging the Galápagos mantle plume with an unconventional application of floating seismometers. Sci Rep, 9: 1326
Pipatprathanporn S, Simons F J. 2021. One year of sound recorded by a mermaid float in the Pacific: Hydroacoustic earthquake signals and infrasonic ambient noise. Geophys J Int, 228: 193–212
Romanowicz B. 2003. Global mantle tomography: Progress status in the past 10 years. Annu Rev Earth Planet Sci, 31: 303–328
Ruan A G, Li J B, Lee C S, Qiu X L, Pan S J. 2012. Passive seismic experiment and ScS wave splitting in the southwestern subbasin of South China Sea. Chin Sci Bull, 57: 3381–3390
Schmandt B, Lin F C. 2014. P and S wave tomography of the mantle beneath the United States. Geophys Res Lett, 41: 6342–6349
Shen W, Ritzwoller M H, Kang D, Kim Y H, Lin F C, Ning J, Wang W, Zheng Y, Zhou L. 2016. A seismic reference model for the crust and uppermost mantle beneath China from surface wave dispersion. Geophys J Int, 206: 954–979
Simmons N A, Myers S C, Johannesson G, Matzel E. 2012. LLNL-G3Dv3: Global P wave tomography model for improved regional and teleseismic travel time prediction. J Geophys Res-Solid Earth, 117: B10302
Simon J D, Simons F J, Irving J C E. 2021a. A MERMAID miscellany: Seismoacoustic signals beyond the P wave. Seismol Res Lett, 92: 3657–3667
Simon J D, Simons F J, Irving J C E. 2021b. Recording earthquakes for tomographic imaging of the mantle beneath the South Pacific by autonomous MERMAID floats. Geophys J Int, 228: 147–170
Simon J D, Simons F J, Nolet G. 2020. Multiscale estimation of event arrival times and their uncertainties in hydroacoustic records from autonomous oceanic floats. Bull Seismol Soc Amer, 110: 970–997
Simons F J, Nolet G, Georgief P, Babcock J M, Regier L A, Davis R E. 2009. On the potential of recording earthquakes for global seismic tomography by low-cost autonomous instruments in the oceans. J Geophys Res-Solid Earth, 114: B05307
Sukhovich A, Bonnieux S, Hello Y, Irisson J O, Simons F J, Nolet G. 2015. Seismic monitoring in the oceans by autonomous floats. Nat Commun, 6: 8027
Sukhovich A, Irisson J O, Simons F J, Ogé A, Hello Y, Deschamps A, Nolet G. 2011. Automatic discrimination of underwater acoustic signals generated by teleseismic P-waves: A probabilistic approach. Geophys Res Lett, 38: L18605
Sweldens W. 1996. The lifting scheme: A custom-design construction of biorthogonal wavelets. Appl Comput Harmonic Anal, 3: 186–200
Tsekhmistrenko M, Sigloch K, Hosseini K, Barruol G. 2021. A tree of Indo-African mantle plumes imaged by seismic tomography. Nat Geosci, 14: 612–619
van der Hilst R D, Widiyantoro S, Engdahl E R. 1997. Evidence for deep mantle circulation from global tomography. Nature, 386: 578–584
Wei S S, Wiens D A, Zha Y, Plank T, Webb S C, Blackman D K, Dunn R A, Conder J A. 2015. Seismic evidence of effects of water on melt transport in the Lau back-arc mantle. Nature, 518: 395–398
Wolfe C J, Solomon S C, Laske G, Collins J A, Detrick R S, Orcutt J A, Bercovici D, Hauri E H. 2009. Mantle shear-wave velocity structure beneath the Hawaiian hot spot. Science, 326: 1388–1390
Xiao H, Xue M, Yang T, Liu C, Hua Q, Xia S, Huang H, Le B M, Yu Y, Huo D, Pan M, Li L, Gao J. 2017. The characteristics of microseisms in South China Sea: Results from a combined data set of OBSs, broadband land seismic stations, and a global wave height model. J Geophys Res-Solid Earth, 123: 3923–3942
Xu W J, Gao M T. 2014. Statistical analysis of the completeness of earthquake catalogs in China mainland (in Chinese). Chin J Geophys,

57: 2802–2812
Yu Y, Chen Y J, Feng Y, An M, Liang X, Guo Z, Qu W, Li S, Dong S. 2021. Asthenospheric flow channel from northeastern Tibet imaged by seismic tomography between Ordos Block and Yangtze Craton. Geophys Res Lett, 48: e93561
Zhang F, Wu Q, Li Y, Zhang R, Sun L, Pan J, Ding Z. 2018. Seismic tomography of Eastern Tibet: Implications for the Tibetan Plateau growth. Tectonics, 37: 2833–2847
Zhao D. 2004. Global tomographic images of mantle plumes and subducting slabs: Insight into deep Earth dynamics. Phys Earth Planet Inter, 146: 3–34
Zhu G, Wiens D A, Yang H, Lin J, Xu M, You Q. 2021. Upper mantle hydration indicated by decreased shear velocity near the southern Mariana Trench from Rayleigh wave tomography. Geophys Res Lett, 48: e93309
Zhu G, Yang H, Lin J, Zhou Z, Xu M, Sun J, Wan K. 2019. Along-strike variation in slab geometry at the southern Mariana subduction zone revealed by seismicity through ocean bottom seismic experiments. Geophys J Int, 218: 2122–2135
Zhu G, Yang H, Lin J, You Q. 2020. Determining the orientation of ocean-bottom seismometers on the seafloor and correcting for polarity flipping via polarization analysis and waveform modeling. Seismol Res Lett, 91: 814–825
Zhu G, Yang H, Yang T, Zhang G. 2023. Along-strike variation of seismicity near the extinct mid-ocean ridge subducted beneath the Manila Trench. Seismol Res Lett, 94: 792–804

(Editorial handling: Ling CHEN)